The Ovuscule

Philippe Thévenaz, *Member*, *IEEE*, Ricard Delgado-Gonzalo, *Student Member*, *IEEE*, and
Michael Unser, *Fellow*, *IEEE*

Abstract—We propose an active contour (a.k.a. snake) that takes the shape of an ellipse. Its evolution is driven by surface terms made of two contributions: the integral of the data over an inner ellipse, counterbalanced by the integral of the data over an outer elliptical shell. We iteratively adapt the active contour to maximize the contrast between the two domains, which results in a snake that seeks elliptical bright blobs. We provide analytic expressions for the gradient of the snake with respect to its defining parameters, which allows for the use of efficient optimizers. An important contribution here is the parameterization of the ellipse which we define in such a way that all parameters have equal importance; this creates a favorable landscape for the proceedings of the optimizer. We validate our construct with synthetic data and illustrate its use on real data as well.

Index Terms—Snakuscule, snake, dynamic contour, ellipse.

✦

---

1 INTRODUCTION

IN a previous paper, we introduced what would possibly be the simplest snake that retains practical usefulness [1]. It was parameterized by just two points, and its purpose was to latch on circular bright image patches. In the present paper, we propose a natural extension whereby the shape of the snake, previously circular, is now allowed to become elliptical. While this upgrade may look trivial conceptually, it is fraught with a surprisingly large increase in the size of the expressions that need to be handled when compared to the circular version. The potential benefit, however, is substantial because ellipses are able to capture two important properties that circles cannot, such as anisotropy and orientation.

Since the circular version was called a snakuscule, we now call our elliptical snake an ovuscule. It preserves features like being a surface snake, where the energy of the snake is driven not by the data under a curve but by the data enclosed by it. We optimize this energy in iterative fashion. More precisely, at each iteration, we want to tune the geometry of the ovuscule to increase the contrast between the intensity of the data averaged over an elliptical core, and the intensity of the data averaged over an elliptical shell—a bigger ellipse from which the elliptical core has been removed, as shown in Fig. 1. If Γ and Γ' represent these elliptical surfaces, with $\Gamma' \subset \Gamma$, and if f represents our image data, then the criterion to minimize is $J = J_{\mathrm{D}} + J_{\mathrm{R}}$, where J_{R} is a contribution due to some regularization term and where the data term J_{D} is given by

$$J_{\mathrm{D}} = \frac{1}{|\Gamma|} \left(\int_{\Gamma \backslash \Gamma'} f(\mathbf{x}) \, \mathrm{d}x_1 \, \mathrm{d}x_2 - \int_{\Gamma'} f(\mathbf{x}) \, \mathrm{d}x_1 \, \mathrm{d}x_2 \right). \quad (1)$$

● *The authors are with the Biomedical Imaging Group, École polytechnique fédérale de Lausanne (EPFL), EPFL/STI/IMT/LIB, Station 17, CH-1015 Lausanne VD, Switzerland.*
E-mail: {philippe.thevenaz, ricard.delgado, michael.unser}@epfl.ch.

There, $|\Gamma|$ is the area of the outer ellipse. To enforce that the criterion remains neutral when f takes a constant value f_0, we maintain $|\Gamma| = 2\,|\Gamma'|$. Under these conditions, $J_{\mathrm{D}}|_{f=f_0} = 0$ does depend neither on the snake nor even on f_0.

This paper is organized as follows: After briefly reviewing the literature on the characterization of ellipses in Section 2, we develop the formalism of our proposed solution in Section 3. We first detail which ellipse parameterization we chose in Section 3.1, and show in Section 3.2 how it is combined with our snake model. We then present in Section 4 how our proposed ovuscule behaves in practice, based on experiments with synthetic and real data, before we finally conclude in Section 5. In the appendices, we provide a few additional relevant properties of ellipses.

2 PREVIOUS WORK

An early example of edge-based ellipse detection can be found in [2], where the coordinates of feature points extracted from an image are submitted to a process based on the Hough transform. A sequence of partial steps is taken to avoid the handling of a 5D space of parameters. Additional variations to take advantage of the Hough transform to detect ellipses have been proposed in [3], [4], [5]; an example of application can be found in [6]. Around the same time, circular spots could be detected by a surface-based method, albeit their size was not adaptive and their location was restricted on the sampling lattice [7].

The use of ellipses as deformable templates was proposed in [8], where it was applied to the detection of vertebral contours, and in [9], where it was applied to ultrasound sequences. Using the snakes of [10] to specifically detect ellipses was first proposed in [11]. There, like in [8], the energy term of the snake ignored surface contributions since it was encouraged to converge to the nearest edge based solely on the gradient of the image. Snakes and Hough transform were combined in [12], where the role of the Hough transform was to provide a convenient elliptical initialization for the snake; the latter, however, was allowed to deviate from an ellipse, and was ignoring surface contributions.

Other early ellipse detection methods concern themselves with the task of fitting *one* ellipse to a discrete set of
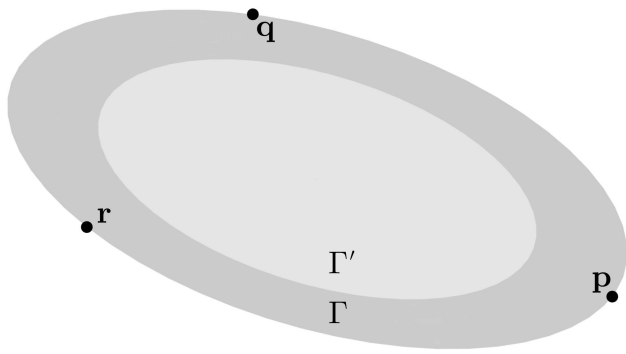
Fig. 1. Two ellipses. The outer ellipse Γ is shown in darker gray; it has an area $|\Gamma|$ that is twice that of the overlaid inner ellipse Γ' shown in lighter gray. These ellipses are entirely determined by the triplet of points $\{\mathbf{p}, \mathbf{q}, \mathbf{r}\}$ that belong to the boundary $\partial\Gamma$ of the outer one.
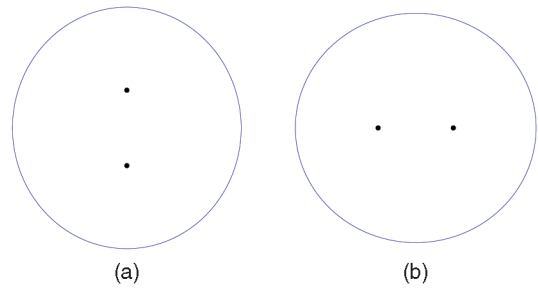

Fig. 2. Ellipses. (a): Tall ellipse. (b): Broad ellipse. These two ellipses of identical area are hard to distinguish because the ratio between their short and long axis is close to unity (it is 95 percent). Yet their associated foci, shown as dots, are far apart.

points. They typically differ in the merit criterion that is optimized [13], [14]. Methods based on surfaces—more precisely, their moments—can also be found in [15], but they require segmented data.

More recently, a spatial Kalman filter was employed in [16] to estimate the parameters of an ellipse represented in polar coordinates, guided by a discrete series of 1D edge detectors irradiating from a seed location. The found ellipse is then tracked through time by a temporal Kalman filter to segment vessels in an ultrasound application. In a revival of Hough-based methods, the authors of [17] suggest that a combination of genetic algorithms with the randomized Hough transform is an appropriate tool to search for several ellipses at once, as opposed to looking for an isolated one. Likewise, the final number of ellipses detected in [18] is determined automatically by a method that involves a surface-based term. It favors the detection of bright elliptical blobs that have the least amount of intensity variation, which is a typical feature of methods based on the Mumford-Shah framework; moreover, overlapping ellipses are avoided. In [19], a collection of salient contour points was extracted from sidescan sonar images to detect mine-like shapes from their acoustic shadow; the six-parameter curves that best fit the data were Lamé curves, a family that includes ellipses. In a strategy that is the reverse of that found in [12], snakes were first applied in [20] to detect contours, and only then was an ellipse fitted to the snake. The purpose was to estimate the rotation of cells.

3 METHOD

3.1 Parameterization

3.1.1 Traditional Characterization of an Ellipse

Gardeners draw an ellipse by attaching a rope of length L to two poles that correspond to its foci; the set of ground locations that can be reached by the rope is an ellipse. More formally, letting $\mathbf{f}_1$ and $\mathbf{f}_2$ be the coordinates of the foci, each coordinate $\mathbf{x}$ of the contour of the ellipse satisfies $\|\mathbf{x} - \mathbf{f}_1\| + \|\mathbf{x} - \mathbf{f}_2\| = L$. This involves five free parameters—two 2D points and a distance.

While this parameterization is easily accessible to intuition, it is, however, not well suited to our task, as hinted at in Fig. 2. For this case, assume that the initial configuration to optimize is that of Fig. 2a, and that the

desired configuration is Fig. 2b. Then, the optimizer is faced with the difficult task of having to apply significant changes to the parameters (the foci of the ellipse) while having only a modest impact on the curve. Meanwhile, it must avoid being deceived by the fact that keeping the foci at a fixed location and operating on L alone can also result in a large variety of elliptical shapes; instead, it must discover by itself that the same L applies to both sides of Fig. 2. In the presence of noise, it is likely that such a configuration favors the appearance of many weak local minima that may stop the optimizer along its path. In conclusion, the traditional parameterization of an ellipse would require an optimizer that is able to cope with interfering parameters of widely different sensitivity.

This problematic aspect of the parameterization above is shared with many other ones that rely on the combination of two points and one scalar, for example, some that would rely on extremal points of the ellipse—those where the curvature is, say, maximal. Since two points define an orientation and since it seems reasonable to ask that this orientation be related in some way to that of the main axis of the ellipse, there will *always* be cases where the optimizer will have to abruptly change this orientation to obtain just a slight change in the ellipse, particularly when its eccentricity is low. The root of the problem underlying any ellipse parameterization where an orientation plays a role is that the orientation of a circle is undefined.

An ellipse is also a member of a family of curves known as quadrics. Turning to their implicit representation and using polynomial equations or their various elaborations to deal with ellipses does not help the optimizer either. This is so because the impact of the various coefficients involved differs widely from one coefficient to the next, due to the fact that each one applies to variables raised to different degrees. Loosely speaking, this inhomogeneous situation results in a highly nonstationary Hessian of the criterion with respect to the parameters, which is hard to optimize.

We have explored alternative ellipse parameterizations, for example, one that associates to a triangle an ellipse of identical inertia and barycenter. But it turned out that interacting with the triangle as a proxy for the ellipse makes for a decidedly nonintuitive control of the ellipse; moreover, messy algebra is involved. To conclude, one of the most delicate aspects of this work lies in the choice of the proper parameterization of an ellipse. We have finally retained the construct that we present in the sequel. It satisfies the following list of requirements in every aspect.

3.1.2 Requirements

Since the initial location of the ovuscule may be given by visual interaction with a human user, our requirements are as follows:

- We want the parameters to be given not by sliders and numbers, but by the coordinates of handles whose location can be controlled graphically by the user in an intuitive way. Because an ellipse is given by five parameters, we need at least three control points in two dimensions. This generates one free parameter that needs to be regularized.

- We want the interaction with the parameters to be natural. Therefore, a parameterization where the control points belong to the ellipse should be favored. In addition, the presence of the free parameter should not lead to counterintuitive behavior.

- The parameterization must be tractable analytically. We need this to be able to predict the variation of the energy of the snake when moving the control points. This requirement rules out many descriptions of an ellipse, particularly those that result in piecewise elliptic segments. Unfortunately, such descriptions are naturally prevalent with ellipses because these curves are quadrics and sooner or later a square root shows up in the derivations. Most often, both the positive and negative cases must be considered, which is highly inconvenient when establishing the value of a gradient.

- We want to be able to determine a rectangular bounding box that is aligned with the system of coordinates and that tightly encloses the ellipse. This allows us to focus our attention to the relevant image data.

- Testing if an arbitrary coordinate belongs to the ellipse area ought to incur a low computational cost. As this operation must be repeated for every pixel of the bounding box when determining the energy of the snake, any reduction in computational complexity there will result in large savings.

- A permutation of the control points should leave the ellipse unchanged. In other words, the role of the control points should be identical. Enforcing that the contributions of each parameter are weighted equally is of great help to the optimizer.

In the remaining part of this paper, we propose a parameterization that retains homogeneity by dealing with points of interchangeable role. We also manage to escape the fact that the orientation of a circle is undefined.

3.1.3 Proposed Solution

Let $\mathbf{A}$ represent an invertible affine transform in two dimensions. To simplify the notations, we use homogenous coordinates so that $\mathbf{A}$ is a (3×3) matrix with six free parameters, two of which do represent the translational part of the transformation. Similarly, 2D coordinates are represented by three-component vectors in $(\mathbb{R}^2 \times \{1\})$. For example, consider the three particular coordinates $\mathbf{c}_0 = (1, 0, 1)$, $\mathbf{c}_1 = (-\frac{1}{2}, \frac{\sqrt{3}}{2}, 1)$, and $\mathbf{c}_2 = (-\frac{1}{2}, -\frac{\sqrt{3}}{2}, 1)$. They determine an equilateral triangle with vertices that belong to the unit circle $\partial\Gamma_{\mathbf{I}}$. It turns out that the curve $\partial\Gamma_{\mathbf{A}}$ resulting from the application of $\mathbf{A}$ to $\partial\Gamma_{\mathbf{I}}$ is the contour of an ellipse.

By construction, the points $(\mathbf{A}\,\mathbf{c}_0)$, $(\mathbf{A}\,\mathbf{c}_1)$, and $(\mathbf{A}\,\mathbf{c}_2)$ belong to $\partial\Gamma_{\mathbf{A}}$.

Our goal now is to invert this mapping. Given three arbitrary—but distinct—points $\mathbf{p} = (p_1, p_2, 1)$, $\mathbf{q} = (q_1, q_2, 1)$, and $\mathbf{r} = (r_1, r_2, 1)$, we want to determine a matrix $\mathbf{A}$ such that $\mathbf{p} = \mathbf{A}\,\mathbf{c}_0$, $\mathbf{q} = \mathbf{A}\,\mathbf{c}_1$, and $\mathbf{r} = \mathbf{A}\,\mathbf{c}_2$. This is a linear system in six unknowns; its solution is $\mathbf{A} = [\mathbf{p}\ \mathbf{q}\ \mathbf{r}]\,[\mathbf{c}_0\ \mathbf{c}_1\ \mathbf{c}_2]^{-1}$. It follows that the area of the ellipse mirrors the area of the unit circle after application of $\mathbf{A}$; it is given by

$$|\Gamma| = \frac{2\,\pi}{\sqrt{27}}\,|\alpha|, \qquad (2)$$

with $\alpha = \det([\mathbf{p}\ \mathbf{q}\ \mathbf{r}])$. As our construction inscribes a triangle within an ellipse, it is the converse of the so-called midpoint ellipse, which inscribes an ellipse within a triangle [21].

3.1.4 Bounding Box

Any point $\mathbf{x}$ of $\partial\Gamma_{\mathbf{A}}$ satisfies the general implicit equation of an ellipse given by $e(\mathbf{x}) = 0$, with

$$e(\mathbf{x}) = e_0 + e_1\,x_1 + e_2\,x_2 + e_{11}\,x_1^2 + e_{12}\,x_1\,x_2 + e_{22}\,x_2^2, \quad (3)$$

where $\{e_i\}$ are the Cartesian parameters of the ellipse which are unique up to a shared multiplicative factor. At the same time, its inverse-transformed version $\boldsymbol{\gamma} = \mathbf{A}^{-1}\,\mathbf{x}$ satisfies the canonic equation of a circle given by $\|\boldsymbol{\gamma} - (0, 0, 1)\|^2 = 1$. By expanding this last equality and by identification in (3) of terms of same power, we have that

$$
\begin{cases}
e_0 = -3\,\big((\mathbf{pq})_1\,p_2\,q_1\,r_2 + (\mathbf{pq})_2\,p_1\,q_2\,r_1\big) \\
\qquad - 3\,\big((\mathbf{qr})_1\,p_2\,q_2\,r_1 + (\mathbf{qr})_2\,p_1\,q_1\,r_2\big) \\
\qquad - 3\,\big((\mathbf{rp})_1\,p_1\,q_2\,r_2 + (\mathbf{rp})_2\,p_2\,q_1\,r_1\big), \\
e_1 = 3\,(p_1 + q_1)\,(p_2\,q_2 - r_2^2) \\
\qquad + 3\,(q_1 + r_1)\,(q_2\,r_2 - p_2^2) \\
\qquad + 3\,(r_1 + p_1)\,(r_2\,p_2 - q_2^2), \\
e_2 = 3\,(p_2 + q_2)\,(p_1\,q_1 - r_1^2) \\
\qquad + 3\,(q_2 + r_2)\,(q_1\,r_1 - p_1^2) \\
\qquad + 3\,(r_2 + p_2)\,(r_1\,p_1 - q_1^2), \\
e_{11} = 3\,(p_2\,(\mathbf{pq})_2 + q_2\,(\mathbf{qr})_2 + r_2\,(\mathbf{rp})_2), \\
e_{12} = 3\,(p_1\,q_2 + p_2\,q_1 - 2\,p_1\,p_2 \\
\qquad + q_1\,r_2 + q_2\,r_1 - 2\,q_1\,q_2 \\
\qquad + r_1\,p_2 + r_2\,p_1 - 2\,r_1\,r_2), \\
e_{22} = 3\,(p_1\,(\mathbf{pq})_1 + q_1\,(\mathbf{qr})_1 + r_1\,(\mathbf{rp})_1),
\end{cases}
\qquad (4)
$$

where

$$
\begin{cases}
(\mathbf{pq}) = \mathbf{p} - \mathbf{q}, \\
(\mathbf{qr}) = \mathbf{q} - \mathbf{r}, \\
(\mathbf{rp}) = \mathbf{r} - \mathbf{p}.
\end{cases}
\qquad (5)
$$

Then, we can easily find a bounding box fitting the orientation of the Cartesian system of coordinates by solving for $e(\mathbf{x}) = 0$ and $\frac{\partial e(\mathbf{x})}{\partial x_i} = 0$ in terms of four extremal points. Setting $i = 1$, we determine that the vertical range of the ellipse is $[g_2 - \frac{2}{\sqrt{27}}\,\sqrt{e_{11}}, g_2 + \frac{2}{\sqrt{27}}\,\sqrt{e_{11}}]$. Setting $i = 2$, we determine that the horizontal range of the ellipse is $[g_1 - \frac{2}{\sqrt{27}}\,\sqrt{e_{22}}, g_1 + \frac{2}{\sqrt{27}}\,\sqrt{e_{22}}]$. There, $\mathbf{g} = \frac{1}{3}\,(\mathbf{p} + \mathbf{q} + \mathbf{r})$ is the barycenter of the ellipse.
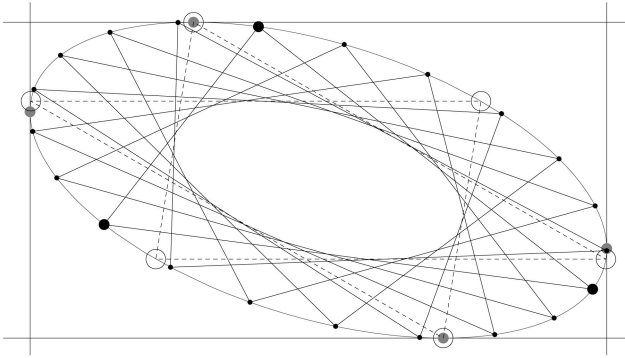
Fig. 3. Ellipse and its bounding box. The four gray dots indicate the location where the bounding box is tangent to the ellipse. The three fat black dots correspond to $\mathbf{p}$, $\mathbf{q}$, and $\mathbf{r}$, in arbitrary order. The remaining thin dots give alternative parameterizations of the same ellipse; they are joined by straight lines so that the corresponding triangles indicate how to group them in sets of three. The dashed lines, along with the hollow circles, give the two parameterizations for which the regularization is optimal (see Section 3.2.6).

3.1.5 Membership

To test for the membership of a point $\mathbf{x}$ to the interior of the ellipse, it is sufficient to consider the sign of $e(\mathbf{x})$. In particular, since an ellipse is a convex shape, we can conclude from the relation $e(\mathbf{g}) = -\alpha^2$ that negative signs must be associated to the interior of the ellipse, and positive signs to its exterior. Since e is a low-degree polynomial, the repeated test for membership of $\mathbf{x}$ to the interior of $\Gamma_{\mathbf{A}}$ comes at a low computational cost once its coefficients have been established. This is even more so once (3) has been rewritten in a system of coordinates centered on $\mathbf{g}$, since $e(\mathbf{y} + \mathbf{g}) = -\alpha^2 + e_{11}\,y_1^2 + e_{12}\,y_1\,y_2 + e_{22}\,y_2^2$, where no linear contribution does appear. Moreover, $e(\mathbf{y} + \mathbf{g}) = e(\mathbf{x})$ for the centered coordinate $\mathbf{y} = \pm(\mathbf{x} - \mathbf{g})$.

3.1.6 Parametric Ambiguity

An ellipse has five degrees of liberty. As we are using three points to describe it, we have six parameters at our disposal since each point comes with two independent coordinates. Therefore, several disjoint combinations of $\{\mathbf{p}, \mathbf{q}, \mathbf{r}\}$ give rise to the same ellipse. This happens because we could have chosen to distribute $\{\mathbf{c}_0, \mathbf{c}_1, \mathbf{c}_2\}$ anywhere on the unit circle while still enforcing them to build an equilateral triangle. Our construction is defined up to some arbitrary rotation.

Because $\{\mathbf{c}_0, \mathbf{c}_1, \mathbf{c}_2\}$ are distributed regularly on the unit circle, $\{\mathbf{p}, \mathbf{q}, \mathbf{r}\}$ retain some regularity on $\partial\Gamma_{\mathbf{A}}$. We illustrate that aspect in Fig. 3, where we observe that our parameterization, while nonunique, feels natural. This impression may be reinforced by the property that the orientation given by the line $\overline{\mathbf{pq}}$ is parallel to the tangent to the ellipse at the opposite vertex $\mathbf{r}$. This property of $\{\mathbf{p}, \mathbf{q}, \mathbf{r}\}$ is inherited from $\{\mathbf{c}_0, \mathbf{c}_1, \mathbf{c}_2\}$.

3.2 Snake

3.2.1 Inner Ellipse

We associate $\{\mathbf{p}, \mathbf{q}, \mathbf{r}\}$ to Γ. Then, the question arises as how to parameterize Γ'. Our requirements are as follows: $|\Gamma'| = \frac{1}{2}\,|\Gamma|$, $\mathbf{g}' = \mathbf{g}$, and the orientation of Γ' must match that of Γ. It can be seen that they are satisfied by setting

$$\begin{cases} e'_0 = \frac{1}{3}\,e_0 + \frac{1}{4}\,((pq)^2 + (qr)^2 + (rp)^2), \\ e'_1 = \frac{1}{2}\,e_1, \\ e'_2 = \frac{1}{2}\,e_2, \\ e'_{11} = \frac{1}{2}\,e_{11}, \\ e'_{12} = \frac{1}{2}\,e_{12}, \\ e'_{22} = \frac{1}{2}\,e_{22}, \end{cases} \tag{6}$$

where

$$\begin{cases} (pq) = p_1\,q_2 - p_2\,q_1, \\ (qr) = q_1\,r_2 - q_2\,r_1, \\ (rp) = r_1\,p_2 - r_2\,p_1. \end{cases} \tag{7}$$

Moreover, we have that $\alpha' = \frac{1}{2}\,\alpha$. This leads to a simple expression for testing the membership of a centered coordinate $\mathbf{y}$ to Γ' which is given by $e'(\mathbf{y} + \mathbf{g}) = \frac{1}{2}\,e(\mathbf{y} + \mathbf{g}) + \frac{1}{4}\,\alpha^2 < 0$. By defining $\rho(\mathbf{y}) = \frac{1}{|\alpha|}\,\sqrt{e(\mathbf{y} + \mathbf{g}) + \alpha^2} = \frac{1}{|\alpha|}\,\sqrt{2\,e'(\mathbf{y} + \mathbf{g}) + \alpha^2/2}$, we see that $\rho(\mathbf{0}) = 0$, $\rho(\mathbf{x} - \mathbf{g}) = 1/\sqrt{2}$ for $\mathbf{x} \in \partial\Gamma'$, and $\rho(\mathbf{x} - \mathbf{g}) = 1$ for $\mathbf{x} \in \partial\Gamma$. Thus, ρ plays the role of a normalized distance between $\mathbf{x}$ and $\mathbf{g}$.

3.2.2 Transitions

While the contrast defined in (1) seems to be a promising energy term, it suffers from a major drawback when computing $\partial J_{\mathrm{D}}/\partial p$, where p is any one of the components of $\{\mathbf{p}, \mathbf{q}, \mathbf{r}\}$, because localized contributions appear along $\partial\Gamma'$ and $\partial\Gamma$ when applying the Leibnitz integral rule to the bounds of the integral. It is our opinion that it would be more appropriate to put these contributions in relation with some 2D surface of f rather than just a 1D curve. Therefore, we want to avoid these localized contributions by building two extended transition zones: one from Γ' to Γ and another from Γ to the exterior of the ovuscule. Naming w the weight that captures the transitions, we rewrite (1) as

$$J_{\mathrm{D}} = \frac{1}{|\Gamma|}\,\int_{\mathbb{R}^2}\,w(\mathbf{x} - \mathbf{g})\,f(\mathbf{x})\,\mathrm{d}x_1\,\mathrm{d}x_2. \tag{8}$$

Our task now is to properly define w. To do so, we propose to take advantage of ρ to devise an index of the "distance" between a coordinate and an ellipse, expressed in the units of $\mathbf{x}$. We first write

$$d'(\mathbf{y}) = \|\mathbf{y}\|\,\left(1 - \frac{1}{\sqrt{2}}\,\frac{1}{\rho(\mathbf{y})}\right). \tag{9}$$

Note that $y_3 = 0$ because $\mathbf{y}$ is the difference of two homogenous coordinates, so that $\|\mathbf{y}\|$ is equivalent to the euclidean norm of the first two components of $\mathbf{y}$. Under the convention that $\partial\Gamma \subset \Gamma'$, we have $d'(\mathbf{x} - \mathbf{g}) = 0$ for $\mathbf{x} \in \partial\Gamma'$; moreover, $d'(\mathbf{x} - \mathbf{g}) \leq 0$ for $\mathbf{x} \in \Gamma'$ and $d'(\mathbf{x} - \mathbf{g}) > 0$ for $\mathbf{x} \notin \Gamma'$. (Unfortunately, we have to note that $\lim_{y_2 \to 0} d'((0, y_2)) \neq \lim_{y_1 \to 0} d'((y_1, 0))$, so that d' has no limit at $\mathbf{y} = \mathbf{0}$ because a function can have at most one limit.) In addition to d', we also define

$$d(\mathbf{y}) = \|\mathbf{y}\|\,\left(1 - \frac{1}{\rho(\mathbf{y})}\right). \tag{10}$$

Similarly, we have $d(\mathbf{x} - \mathbf{g}) = 0$ for $\mathbf{x} \in \partial\Gamma$; moreover, $d(\mathbf{x} - \mathbf{g}) \leq 0$ for $\mathbf{x} \in \Gamma$ and $d(\mathbf{x} - \mathbf{g}) > 0$ for $\mathbf{x} \notin \Gamma$. (Again, $\lim_{y_2 \to 0} d((0, y_2)) \neq \lim_{y_1 \to 0} d((y_1, 0))$, but this is now irrelevant because we are not going to pay attention to d anywhere inside Γ'.) We finally define w as

$$w(\mathbf{y} + \mathbf{g})$$

$$= \begin{cases} -1, & d'(\mathbf{y}) < -\frac{1}{\sqrt{2}}, & \mathrm{I}, \\ \sqrt{2}\, d'(\mathbf{y}), & -\frac{1}{\sqrt{2}} \leq d'(\mathbf{y}) < \frac{1}{\sqrt{2}}, & \mathrm{II}, \\ 1, & \frac{1}{\sqrt{2}} \leq d'(\mathbf{y}) \wedge d(\mathbf{y}) < -1, & \mathrm{III}, \\ \frac{1}{2}\,(1 - d(\mathbf{y})), & -1 \leq d(\mathbf{y}) < 1, & \mathrm{IV}, \\ 0, & 1 \leq d(\mathbf{y}), & \mathrm{V}. \end{cases} \quad (11)$$

Conflicting conditions may arise in (11), especially when we have, at the same time, $d'(\mathbf{y}) < \frac{1}{\sqrt{2}}$ and $-1 \leq d(\mathbf{y})$. Since this state of affairs only corresponds to cases where the ovuscule is stretched thin, we shall not further it.

An interesting property of w reveals itself when we consider the simplified case of Γ being a disk of radius R. Under a suitable translation and orientation of the system of coordinates, we have that $\{\mathbf{p}, \mathbf{q}, \mathbf{r}\} = R\,\{\mathbf{c}_0, \mathbf{c}_1, \mathbf{c}_2\}$. Then, $\rho(\mathbf{y}) = \frac{1}{R}\,\|\mathbf{y}\|$, along with $d'(\mathbf{y}) = \|\mathbf{y}\| - R/\sqrt{2}$ and $d(\mathbf{y}) = \|\mathbf{y}\| - R$. For neutral data characterized by $f = f_0$, it follows that

$$\begin{aligned} J_\mathrm{D} = \frac{f_0}{\pi\,R^2} \int_{-\pi}^{\pi} & \left(\int_0^{\frac{R}{\sqrt{2}} - \frac{1}{2}} (-1)\, r\, \mathrm{d}r \right. \\ & + \int_{\frac{R}{\sqrt{2}} - \frac{1}{2}}^{\frac{R}{\sqrt{2}} + \frac{1}{2}} \sqrt{2}\, \left(r - \frac{R}{\sqrt{2}} \right) r\, \mathrm{d}r + \int_{\frac{R}{\sqrt{2}} + \frac{1}{2}}^{R-1} (1)\, r\, \mathrm{d}r \\ & \left. + \int_{R-1}^{R+1} \frac{1}{2}\, (1 - r + R)\, r\, \mathrm{d}r \right) \mathrm{d}\vartheta \\ = 0. \end{aligned} \quad (12)$$

Since J_D depends neither on R nor on f_0 when $\{\mathbf{p}, \mathbf{q}, \mathbf{r}\}$ forms an equilateral triangle, the optimizer will not favor one configuration over another, even after the zones of transition have been introduced, which is the desired behavior.

3.2.3 Sampling

Invariably in image processing, the continuously defined image $f(\mathbf{x})$ in (8) is given by its discrete samples $f[\mathbf{k}]$. Although it would be possible in principle to build a continuously defined model to estimate $f(\cdot)$ given $f[\cdot]$, this is highly impractical because it would lead to intractable integrals. Instead, we propose replacing (8) by the sampled version given by

$$J_\mathrm{D} = \frac{1}{|\Gamma|} \sum_{\mathbf{k} \in \mathbb{Z}^2} w(\mathbf{k})\, f[\mathbf{k}], \quad (13)$$

where w is computed as before and where $|\Gamma|$ is given in (2). The range of indices $\mathbf{k}$ that need to be explored can be made finite by applying the considerations of Section 3.1.4. Moreover, because an ellipse always retains a convex shape, further acceleration is possible within Domains I and III of (11) if one takes advantage of Green's theorem. We show in Fig. 4 how the conditions in (11) have to be applied in the case of an arbitrary ovuscule.

3.2.4 Justification of the Domains of Transition

We introduced in Section 3.2.2 a specific weighting function w and argued that, even in the continuous case (8), it is desirable to design domains of transition to avoid the localized effect of the Leibnitz integral rule. In the sampled case, however, the Leibnitz integral rule does not apply;
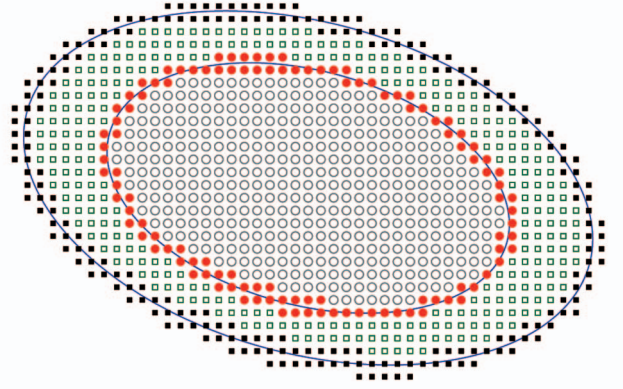

Fig. 4. Repartition of the contributions to w. Domain I, circles: $d' < -1/\sqrt{2}$. Domain II, disks: transition zone $-1/\sqrt{2} \leq d' < 1/\sqrt{2}$. Domain III, hollow squares: $d < -1$. Domain IV, filled squares: transition zone $-1 \leq d < 1$.

nevertheless, we argue in this section that establishing domains of transition is even more important. Indeed, in their absence, and because of the sampling mechanism, an infinitesimal change in the parameters of the ovuscule would sometimes result in an abrupt swap of the membership of the coordinate $\mathbf{k}$ to either Γ', Γ, or $(\mathbb{R}^2 \backslash \Gamma)$. In turn, this swap would lead to discontinuities in the criterion. We now illustrate how our design of w restores a state that is easier to optimize.

We start by observing that (13) can be rewritten as $J_\mathrm{D} = f_0\, W + \frac{1}{|\Gamma|} \sum_{\mathbf{k} \in \mathbb{Z}^2} w(\mathbf{k})\, (f[\mathbf{k}] - f_0)$ for any $f_0 \in \mathbb{R}$, with $W = \frac{1}{|\Gamma|} \sum_{\mathbf{k} \in \mathbb{Z}^2} w(\mathbf{k})$. Obviously, the term W depends on geometry alone; moreover, the condition $W = 0$ is the only one that satisfies our fundamental requirement that J_D be dependent only on the contrast between the data under Γ and $(\Gamma \backslash \Gamma')$, and not on any intensity offset f_0. (Allow us to recall here that enforcing $|\Gamma| = 2\,|\Gamma'|$ along with $w^\mathrm{I} = -1$, $w^\mathrm{III} = 1$, and $w^\mathrm{V} = 0$ makes for a consistent approach as far as (8) is concerned.)

For the sake of the argument, we temporarily delete the zones of transition II and IV and dole out the reclaimed area to Domains I, III, and V. This results in w taking discrete values in $\{-1, 1, 0\}$, delimited by the conditions $d'(\mathbf{y}) < 0$, $0 \leq d'(\mathbf{y}) \wedge d(\mathbf{y}) < 0$, and $0 \leq d(\mathbf{y})$, respectively. Consider now optimizing J_D around some initial condition $\{\mathbf{p}, \mathbf{q}, \mathbf{r}\}$, for instance, by exploring a range of values around one component, say, by perturbing r_2 by Δr. Thus, despite changes in the exploration parameter Δr that remain continuous, some integer coordinates $\mathbf{k}$ in (13) may experience in the transitionless case an abrupt swap of domain membership. We illustrate in Fig. 5 the impact of these changes on W for the arbitrary ovuscule defined by $\mathbf{p} = (-20, 10, 1)$, $\mathbf{q} = (5, -12, 1)$, and $\mathbf{r} = (18, 7 + \Delta r, 1)$, with $\Delta r \in [-2, 2]$. (Incidentally, the ovuscule of Fig. 4 corresponds to $\Delta r = 0.3$.)

We see that the resulting W_0 takes an agitated appearance, with many local minima that may potentially interfere with the data-related minimum we are seeking. If that function would be piecewise constant, the situation would be less dramatic because at least the gradient $\mathrm{d}W_0/\mathrm{d}\Delta r$ would
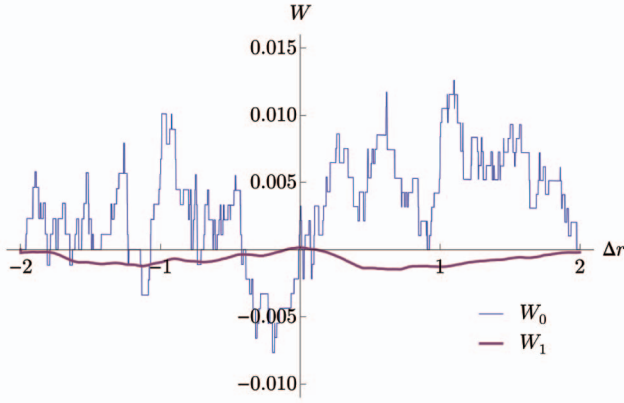
Fig. 5. Effect of sampling with and without zones of transition. Thin graph W_0: Shrinking Domains II and IV to vanishing size leads to a discontinuous w and ultimately to a discontinuous J_D. Thick graph W_1: Defining w as in (11) leads to a continuous w and ultimately to a continuous J_D. The graphs W capture the combined effect of geometry and sampling; they do not depend on data.

vanish almost everywhere, but that is not even the case in view of the normalization factor $1/|\Gamma|$. Meanwhile, the function W_1 corresponds to the nominal case (11), with all domains of transition restored. Their benefit is essentially to provide for a fuzzy membership that smoothes out the swap between domains. Clearly, the number of local minima has much abated; moreover, the approximation of the desired condition $W = 0$ is strikingly better for W_1 than for W_0.

3.2.5 Optimization

Many optimizers are at one's disposal to search for the minimum value taken by (13). Some of them require the calculation of the gradient of J_D with respect to the components of $\{\mathbf{p}, \mathbf{q}, \mathbf{r}\}$, such as the conjugate gradient-based method that we use in this paper. In this section, we are going to build an expression of the gradient $\boldsymbol{\nabla} J_D = (\partial J_D/\partial p_1, \partial J_D/\partial p_2, \partial J_D/\partial q_1, \partial J_D/\partial q_2, \partial J_D/\partial r_1, \partial J_D/\partial r_2)$ by examining each domain of (11) independently. Following lengthy calculations[1] and defining the 6D vector

$$(\mathbf{pqr}) = ((\mathbf{qr})_2, -(\mathbf{qr})_1, (\mathbf{rp})_2, -(\mathbf{rp})_1, (\mathbf{pq})_2, -(\mathbf{pq})_1), \quad (14)$$

we find that

$$\boldsymbol{\nabla} J_D^{\mathrm{I}} = \frac{1}{\alpha\,|\Gamma|} \sum_{\mathbf{k} \in \Omega^{\mathrm{I}}} f[\mathbf{k}]\,(\mathbf{pqr}), \quad (15)$$

where Ω^{I} corresponds to Domain I of w. Meanwhile, over Domain II, we have that

$$\boldsymbol{\nabla} J_D^{\mathrm{II}} = -\frac{1}{\alpha\,|\Gamma|} \sum_{\mathbf{k} \in \Omega^{\mathrm{II}}} f[\mathbf{k}]\,\|\mathbf{y}\| \left(\sqrt{2}\,(\mathbf{pqr}) + \frac{1}{6\,\alpha\,\rho^3} \right.$$
$$(-y_2\,h_1 + u_1, y_1\,h_1 + u_2, -y_2\,h_2 + u_1, \quad (16)$$
$$\left. y_1\,h_2 + u_2, -y_2\,h_3 + u_1, y_1\,h_3 + u_2) \right),$$

with $\mathbf{y} = \mathbf{k} - (g_1, g_2)$, with

$$\begin{cases} u_1 = \left(2\,e_{11} + \sqrt{8}\,\alpha^2\,d'(\mathbf{y})\,\frac{\rho^3}{\|\mathbf{y}\|^3} \right) y_1 + e_{12}\,y_2, \\ u_2 = \left(2\,e_{22} + \sqrt{8}\,\alpha^2\,d'(\mathbf{y})\,\frac{\rho^3}{\|\mathbf{y}\|^3} \right) y_2 + e_{12}\,y_1, \end{cases} \quad (17)$$

and with

$$\mathbf{h} = \begin{cases} 9\,(((\mathbf{rp})_2 - (\mathbf{pq})_2)\,y_1 - ((\mathbf{rp})_1 - (\mathbf{pq})_1)\,y_2), \\ 9\,(((\mathbf{pq})_2 - (\mathbf{qr})_2)\,y_1 - ((\mathbf{pq})_1 - (\mathbf{qr})_1)\,y_2), \\ 9\,(((\mathbf{qr})_2 - (\mathbf{rp})_2)\,y_1 - ((\mathbf{qr})_1 - (\mathbf{rp})_1)\,y_2). \end{cases} \quad (18)$$

Over Domain III, we find that

$$\boldsymbol{\nabla} J_D^{\mathrm{III}} = -\frac{1}{\alpha\,|\Gamma|} \sum_{\mathbf{k} \in \Omega^{\mathrm{III}}} f[\mathbf{k}]\,(\mathbf{pqr}), \quad (19)$$

while, over Domain IV, we write that

$$\boldsymbol{\nabla} J_D^{\mathrm{IV}} = \frac{1}{\alpha\,|\Gamma|} \sum_{\mathbf{k} \in \Omega^{\mathrm{IV}}} f[\mathbf{k}] \left(\frac{\|\mathbf{y}\| - 1}{2}\,(\mathbf{pqr}) + \frac{\|\mathbf{y}\|}{12\,\alpha\,\rho^3} \right.$$
$$(-y_2\,h_1 + v_1, y_1\,h_1 + v_2, -y_2\,h_2 + v_1, \quad (20)$$
$$\left. y_1\,h_2 + v_2, -y_2\,h_3 + v_1, y_1\,h_3 + v_2) \right),$$

with

$$\begin{cases} v_1 = \left(2\,e_{11} + 2\,\alpha^2\,d(\mathbf{y})\,\frac{\rho^3}{\|\mathbf{y}\|^3} \right) y_1 + e_{12}\,y_2, \\ v_2 = \left(2\,e_{22} + 2\,\alpha^2\,d(\mathbf{y})\,\frac{\rho^3}{\|\mathbf{y}\|^3} \right) y_2 + e_{12}\,y_1. \end{cases} \quad (21)$$

Finally, the overall gradient is given by summing the partial contributions found in (15), (16), (19), and (20).

3.2.6 Regularization

We have seen in Section 3.1.6 that the configuration of parameters that minimizes (13) is not unique. To help the optimizer settle in a well-defined solution, we propose to add to J_D the regularization term defined as

$$J_R = \frac{\lambda}{|\Gamma|}\,\min\!\left((\mathbf{pq})_2^2, (\mathbf{qr})_2^2, (\mathbf{rp})_2^2 \right), \quad (22)$$

where λ is some positive regularization weight arbitrarily chosen. Among all equivalent configurations $\{\mathbf{p}, \mathbf{q}, \mathbf{r}\}$ that minimize J_D, our regularization promotes a layout where one side of the triangle $\triangle(\mathbf{p}, \mathbf{q}, \mathbf{r})$ is horizontal. We observe in Fig. 3 that two solutions exist. Thanks to J_R, the optimizer will settle in one of them; which one depends on the conditions that prevailed at the start of the optimization.

We provide the gradient of the regularization with respect to the components of $\{\mathbf{p}, \mathbf{q}, \mathbf{r}\}$ below. We give the three forms that correspond to the selection process in (22)

$$(\mathbf{pq})_2^2 < \min\!\left((\mathbf{qr})_2^2, (\mathbf{rp})_2^2 \right) : \boldsymbol{\nabla} J_R$$
$$= \frac{\lambda}{\alpha|\Gamma|}\,(\mathbf{pq})_2\,(2\,\alpha\,(0, 1, 0, -1, 0, 0) - (\mathbf{pq})_2\,(\mathbf{pqr})), \quad (23)$$

---

1. After simplifications have been applied by a symbolic manipulation software such as `Mathematica`, the gradient of (13) would still require no less than 22 pages to print. The version that we present here is certainly more compact.

TABLE 1
Remapping of Phantom Intensities

Original	Ours
0.00	255
1.00	128
1.01	102
1.02	77
1.03	51
1.04	26
2.00	0

$$(\mathbf{qr})_2^2 < \min\big((\mathbf{rp})_2^2, (\mathbf{pq})_2^2\big) : \boldsymbol{\nabla} J_{\mathrm{R}}$$
$$= \frac{\lambda}{\alpha \, |\Gamma|} \, (\mathbf{qr})_2 \, (2 \, \alpha \, (0,0,0,1,0,-1) - (\mathbf{qr})_2 \, (\mathbf{pqr})),$$
(24)

$$(\mathbf{rp})_2^2 < \min\big((\mathbf{pq})_2^2, (\mathbf{qr})_2^2\big) : \boldsymbol{\nabla} J_{\mathrm{R}}$$
$$= \frac{\lambda}{\alpha|\Gamma|} \, (\mathbf{rp})_2 \, (2 \, \alpha \, (0,-1,0,0,0,1) - (\mathbf{rp})_2 \, (\mathbf{pqr})).$$
(25)

4 EXPERIMENTS

We present in this section four experimental setups. In the two first cases, we can perform an objective validation because we know the ground truth. In the third case, the ground truth is not known, but the shapes to detect are true ellipses. In the last case, the shapes that we want found by the ovuscules are mere approximations of ellipses.

4.1 Robustness to Photometric Noise

To objectively validate the performance of our method in the presence of noise, we propose taking advantage of a phantom of size (512×512) built out of known ellipses. Specifically, we want to recover Ellipse d of the widely used Shepp-Logan phantom [22], with varying degrees of additive white Gaussian noise. To comply with the fact that ovuscules detect bright ellipses, we have remapped the intensities of the original phantom as indicated in Table 1. We show in Fig. 6 the visual outcome of this experiment, with ovuscules in bright. We have enforced the initial position of the ovuscule—that is, before optimization—to always be the same throughout the experiments; we show it in the top-left corner of Fig. 6, along with noiseless data. The remaining images are increasingly noisy; the standard deviation of the noise is $\{10, 20, 50, 100, 200\}$, which corresponds to a signal-to-noise ratio of $\{38, 26, 10, -1, -13\}$ dB, respectively. We see that even when there is a high amount of noise, ovuscules manage to converge on the desired optimum, in spite of the perturbations created by the other ellipses.

As an objective measure of accuracy, we propose computing the Jaccard similarity coefficient $S = |\Gamma' \cap \Theta|/|\Gamma' \cup \Theta|$, where Θ represents the ellipse of reference. To distinguish the robustness to noise from the robustness to the presence of confounding features (which would otherwise bias S), we have simplified the original phantom by retaining only Ellipse d of [22], with intensity 128 over a background of intensity 0. For each given amount of noise, we have generated 100 realizations. We report in Table 2 the outcome
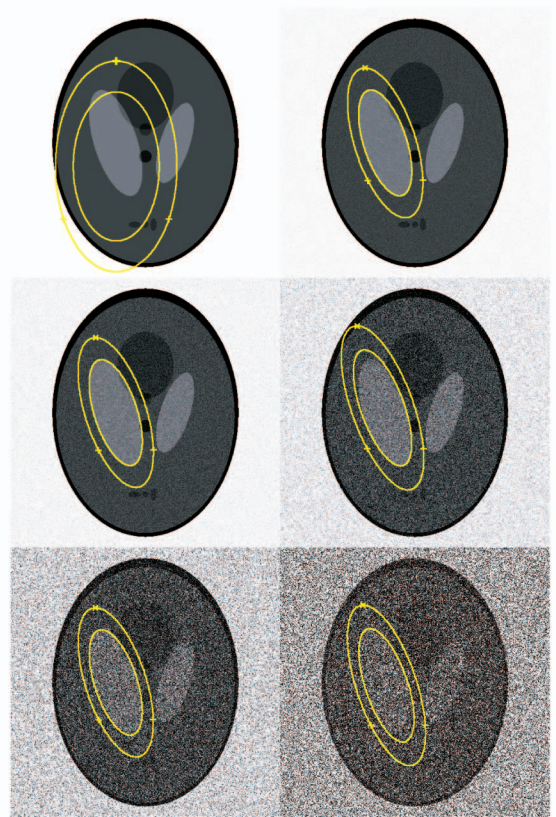

Fig. 6. Application of ovuscules to synthetic data.

of this experiment, where σ is the standard deviation of the noise.

We see that the Jaccard index never reaches exactly the perfect value $S = 1.0$, even in the absence of noise. This is due in part to the fact that the image is not really noiseless since it is but a sampled version of the ideal, continuously defined ground truth. However, we believe that this discrepancy is irrelevant in practice since no more than 18 out of 13,506 pixels are in error, which corresponds to only about 0.1 percent. On the bright side of things, adding copious amounts of noise results in just a modest degradation of the parameters identified by the ovuscule. We show in Fig. 7 one realization for $\sigma = 200$, a large amount of noise[2] for which the good value reached by the Jaccard index indicates that the ovuscule is still in excellent agreement with the ground truth. Adding more noise, however, populates the criterion (13) with local minima in which the ovuscule gets sometimes trapped during the iterative optimization, as confirmed by the last row of Table 2.

4.2 Robustness to Initial Conditions

It is unusual to know beforehand the orientation or elongation of the ellipses we want to capture. In this

2. Because the size of the image has been adjusted to fit the printing space, interpolation has created correlations between pixels, ultimately resulting in reduced apparent noise. Moreover, the dithering inherent in the printing process has brought yet additional doctoring of the image. Finally, the human visual system itself is happy to create illusory boundaries. Altogether, this explains why the contrast of the magnified inset seems so poor in comparison with the apparent contrast of the full-size image. Yet, the procedure we followed to obtain the pixels of the inset was no more involved than simple pixel replication.

TABLE 2
Jaccard Similarity Coefficient

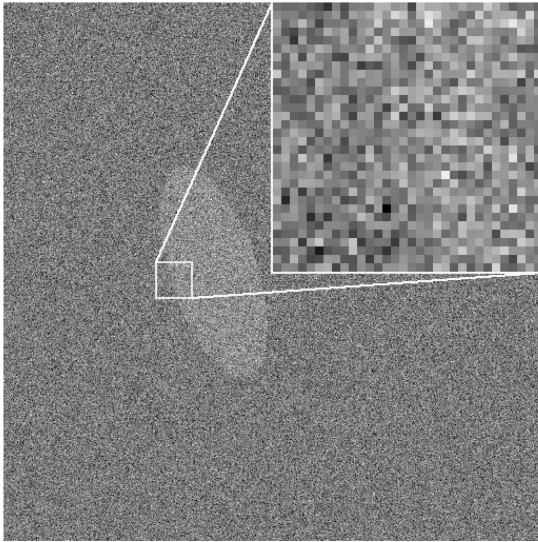| σ	S	$\pm \sigma_S$
0	0.998668	± 0
10	0.998664	± 0.00024
20	0.99865	± 0.00030
50	0.9982	± 0.00051
100	0.997	± 0.0010
200	0.994	± 0.0019
500	0.78	± 0.18

Fig. 7. Noisy realization of Ellipse d. The range of displayed intensities here is $[-3\,\sigma, 255 + 3\,\sigma]$ with $\sigma = 200$. The inset shows a magnification of a (32×32) area to highlight the profusion of noise.

section, we focus on the impact of a mismatch between the initial configuration of an ovuscule and that of its desired target. We also take advantage of this experiment to compare our parameterization to an alternative one; we conclude that the latter is less robust than ours. Moreover, we show in the process that a good initialization strategy is to choose an ovuscule with a circular shape.

4.2.1 Set of Ellipses

We have built a set of ellipses that share area and barycenter, but differ in orientation and elongation. Letting a and b be their semimajor and semiminor axes, we have generated shapes that span (in geometric steps of ratio $2^{1/12}$) a range from the circle $a = r = b$ to the elongated case $\frac{a}{2} = r = 2\,b$, and considered every tilt $\phi \in [0, \pi)$ of the main axis of the ellipse with respect to the horizontal, in arithmetic steps of $\frac{\pi}{36}$. We have synthesized images of size (256×256) with $r = 35$ as all-or-nothing sampled representations, with foreground $f_0 = 100$ and background 0. Thus, for any of these $468 = 13 \times 36$ ellipses, the desired optimal J_D in (1) takes the value $J_0 = -\frac{1}{2}\,f_0$. To accommodate for some deviation, we have defined an ovuscule to be successful if, after optimization, it settles in a configuration for which $\frac{105}{100}\,J_0 \leq J_D \leq \frac{95}{100}\,J_0$.
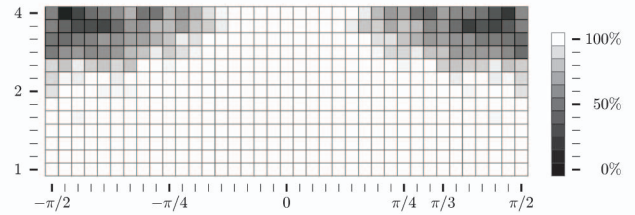

Fig. 8. Intensity-coded success rate of the proposed parameterization, as a function of the mismatch $(\varphi - \phi)$ and of the elongation $\frac{a}{b}$.
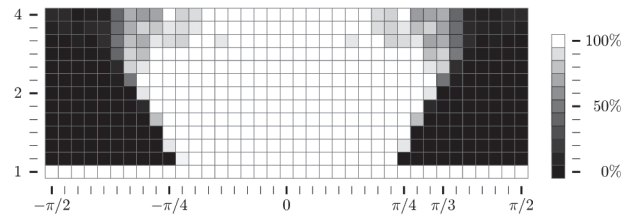

Fig. 9. Intensity-coded success rate of an alternative parameterization, as a function of the mismatch $(\varphi - \phi)$ and of the elongation $\frac{a}{b}$.

4.2.2 Orientation Mismatch

We have launched ovuscules of orientation φ on ellipses of tilt ϕ. In Fig. 8, successes are displayed in bright and failures in dark, with the mismatch $(\varphi - \phi)$ shown in the horizontal axis, and the elongation $\frac{a}{b}$ in the vertical axis. We have explored 13 elongations and 36 mismatches $(\varphi - \phi)$ per elongation. Except for φ and ϕ, each initial parameter (elongation included) was set identical to that of the target ellipse.

We have repeated this experiment with a different way to parameterize the ovuscule. While Fig. 8 corresponds to the parameterization $\{\mathbf{p}, \mathbf{q}, \mathbf{r}\}$ proposed in this paper, Fig. 9 corresponds to the alternative parameterization $\{\mathbf{g}, a, b, \phi\}$ that represents an ellipse by its center, length of semimajor and semiminor axes, and tilt. Comparing Figs. 8 and 9, we see that $\{\mathbf{p}, \mathbf{q}, \mathbf{r}\}$ clearly outperforms $\{\mathbf{g}, a, b, \phi\}$.

We illustrate in Fig. 10 a typical configuration for $\varphi - \phi = \frac{\pi}{3}$, with $\varphi = \frac{\pi}{6}$ and $\phi = -\frac{\pi}{6}$. It is comforting to observe that the failure cases of our parameterization correspond better to what one would consider to be the harder task: They appear only when the amount of initial overlap is limited. By contrast, the logic driving the failure cases observed with $\{\mathbf{g}, a, b, \phi\}$ is less intuitive.

4.2.3 Elongation Mismatch

In practice, not only the orientation, but also the elongation of the elliptical blobs is unknown. Then, we propose to initialize ovuscules as disks. We show the outcome in Fig. 11, where the success rate ρ, averaged over 13 elongations, is given in terms of the target tilt ϕ. We observe that our proposed parameterization now always succeeds, while the alternative one fails nearly half of the time. We finally conclude that applying a circular initialization to our $\{\mathbf{p}, \mathbf{q}, \mathbf{r}\}$ parameterization achieves the best robustness in all cases, restoring success even to the failure cases of Section 4.2.2.
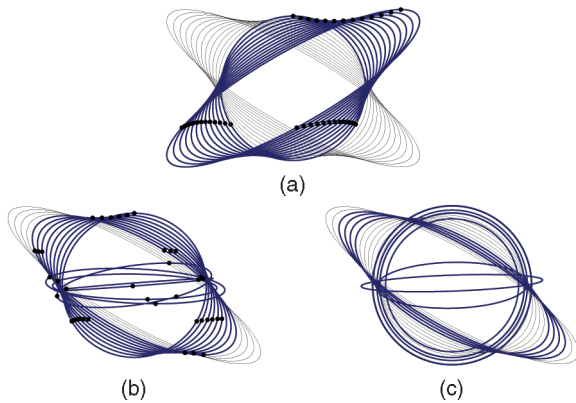
Fig. 12. Ovuscules before optimization.

Fig. 10. Initial configuration for an angular mismatch of $\frac{\pi}{3}$, and final configurations. (a) The 13 thin ellipses depict the desired target configuration, and the thick ellipses give the initial one, with $\{\mathbf{p}, \mathbf{q}, \mathbf{r}\}$ shown as black dots. (b) Our proposed parameterization succeeds nine times. (c) The $\{\mathbf{g}, a, b, \phi\}$ parameterization succeeds five times only.

4.3 Steel Needles

A mixture of steel needles and concrete has been prepared. The needles are cylindrical rods of identical diameter and length. Then, a slab of this reinforced concrete has been cut, polished, and photographed. (The final purpose of the imaging experiment was to characterize how the steel needles did mix with the concrete, in particular their orientation and distribution [23].) Since the intersection of the plane of the cut with a cylindrical needle takes the shape of an ellipse, ovuscules are particularly appropriate tools for the task.

The needles appear as bright material over a darker background; thus, we first detected their approximate location by applying a coarse smoothing to the original image and by detecting the location of strong maxima. On the nonsmoothed image, we then placed one ovuscule per local maximum; we chose its initial shape to be a circle, and its initial radius to be slightly larger than the known radius of the needles. We show in Fig. 12 this initial configuration. We then let the ovuscules evolve. The outcome can be observed in Fig. 13, where we see qualitatively that they manage to fit tightly the profile of the steel needles. Over the whole image (of which only a cutout is shown in Figs. 12 and 13), we detected 191 maxima. On average, the computational time spent while optimizing an ovuscule was 166 ± 106 ms, for a code written in Java on a Mac Pro 2×2.8 GHz Quad-Core Intel Xeon.
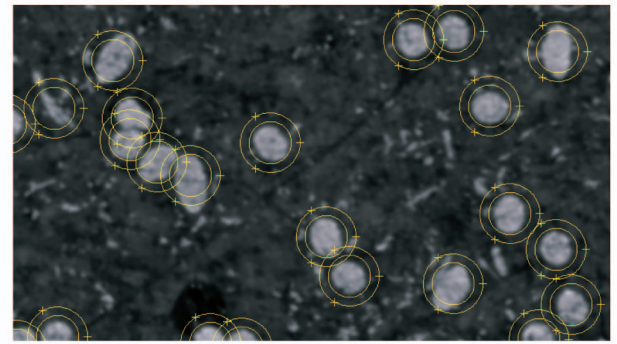
As a more quantitative measure, we found that the average length of the semiminor axis of Γ' is 20.4 ± 3.6 in pixel units. Although some of the detected maxima could not be associated with a needle, the result above includes all measurements, except for eight cases that correspond to degenerate ellipses of vanishing area. Moreover, if we reject as additional outliers the 23 cases where the semiminor axis is either too small or too large, with respective bounds 17 and 24, then the standard deviation of the 160 remaining ovuscules drops down from 3.6 to 0.9, which is indicative of subpixel accuracy.

4.4 Yeast Cells

Yeast cells have been extensively studied by biologists. Within the interphase stage of the cell cycle, their shape is known to be elliptical; during the division stage, the main body of the mother cell and the budding daughter cell can be approximated by a combination of elliptical shapes. However, these characterizations are but idealizations of the true shapes of these cells, which depart from perfect ellipses or the combination thereof. Moreover, the yeast cells we would like to segment do not adhere strictly to the ovuscule requirements of a bright object on a dark background. Luckily, when examined by phase-contrast microscopy and after video inversion to exchange bright for dark, the cells are typically surrounded by some dark halo which can be best discerned in the interphase stage shown in Fig. 14. The contrast provided by this halo helps the ovuscule to converge.
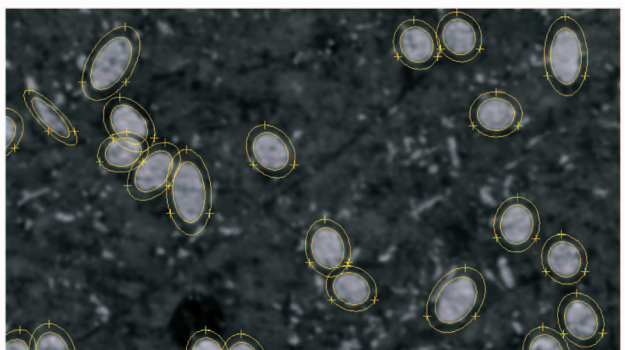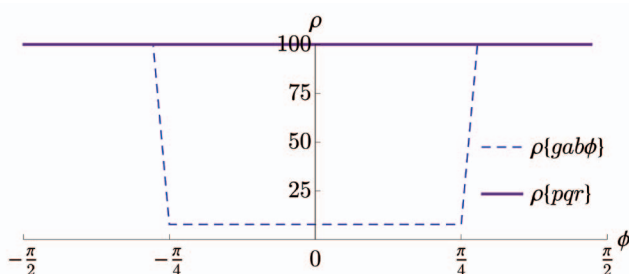

Fig. 11. Success rate ρ in terms of the tilt ϕ of the target ellipse, for a circular initialization. Thick curve: Proposed parameterization. Thin dashed curve: Alternative parameterization.

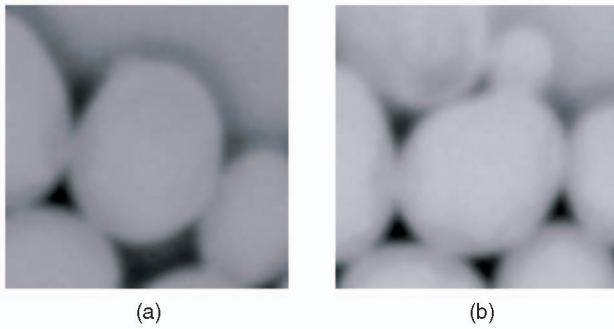
Fig. 13. Ovuscules after optimization.

Fig. 14. Yeast cells. (a) Interphase. (b) The same cell during the division stage of the cell cycle, with a budding daughter cell in the upper part of the image.

Using a similar strategy as in Section 4.3, we initialize the center of the ovuscules by first applying a detector of local maxima to Mexican hat-filtered data, as specified in Appendix A. For crowded yeast cells, however, the initial radius is critical to obtaining a good segmentation. When this initial radius is too big, the ovuscule is influenced by unwanted contribution of surrounding cells in addition of those of the desired cell; during subsequent optimization, the ovuscule is often attracted to a cluster of cells instead of a single one. On the other hand, when the radius is too small, the ovuscule can miss the halo and converge to small features of the cell, or even collapse. In this application, it is therefore advantageous to first launch a high number of ovuscules that are initially circular and cover some range of sizes and to sort them out after they have converged. We show the initialization in Fig. 15 and the corresponding result of the optimization process in Fig. 16. These images represent a small cutout of a much larger image, over which we launched 2,298 ovuscules; each took on average 12 ± 34 ms to complete optimization. This duration is shorter than in the conditions experienced in Section 4.3 because the cells are now smaller and because there is a greater number of failures—which can be detected early during the optimization process.

Once a given cell has been properly segmented within some frame, we can propagate each segment as initial condition for the next frame while tracking a time-sequence of evolving cells. We have observed that ovuscules are quite robust in terms of domain of attraction and keep snapped to
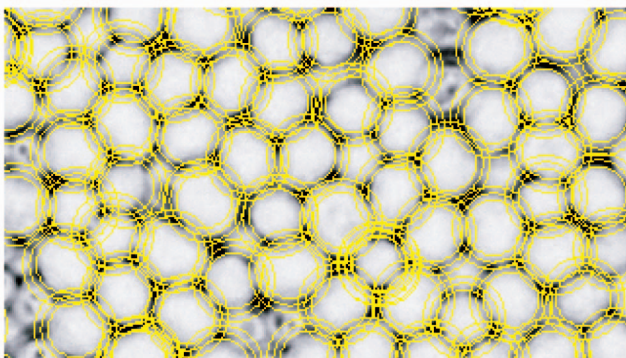

Fig. 15. Yeast cells and initial ovuscules, which come in three sizes. The inversion of contrast allows the cells to appear brighter than their surroundings. To reduce clutter, only $\partial \Gamma'$ is shown as a bright overlay.
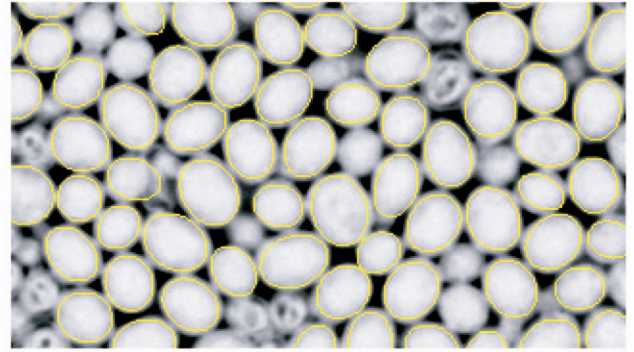

Fig. 16. Yeast cells and final ovuscules. We retain only those ovuscules that survive a pruning process that discards overlapping solutions, dwarf and giant ovuscules, nonrealistic aspect ratios, and insufficient contrast J. The contrast threshold has been chosen to aid in rejecting dead cells—those that exhibit a less-smooth pattern of intensity.

the same target, even under adverse conditions such as spatial displacements and changes in the brightness or shape of the cell. Thus, ovuscules provide effective means to analyze a video sequence of dividing cells. This is especially true for yeast cells, as those divide in a very particular manner: A small bud starts growing on the surface of the mother and eventually becomes a new cell. Therefore, the fundamental original shape of the mother is not altered through time. This behavior encourages the ovuscule to track always the same mother cell.

5 CONCLUSION

We have proposed a dynamic curve that takes the shape of an ellipse; we call it an ovuscule. It is parameterized by three points that belong to the boundary of the ellipse. We have associated to this curve an energy term that is surface-based and that measures the contrast between the interior of the ellipse and its exterior; therefore, ovuscules can be used to detect elliptical bright blobs over a dark background. We have proposed a discretization scheme that leads to a well-defined gradient of the energy with respect to the parameters of the curve, for which we have provided explicit expressions. We have implemented our construction and shown with synthetic experiments that it is robust to noise and to mismatched initial conditions. In addition, we have shown on real data that ovuscules are also impervious to departures from elliptical shape.

APPENDIX A

MEXICAN HAT

Let us write in 2D the impulse response n of a normalized centered Gaussian filter of isotropic variance σ^2 as

$$n(\mathbf{x}, \sigma) = \frac{1}{\sigma^2 \, 2 \, \pi} \, e^{-\frac{\|\mathbf{x}\|^2}{2 \, \sigma^2}}.$$

We preserve its circular symmetry by building our Mexican hat filter m as the difference of two Gaussians given by

$$m(\mathbf{x}, \sigma) = \frac{\pi \, \sigma^2}{\log(2)} \left(n\left(\mathbf{x}, \frac{\sigma}{\sqrt{\log(16)}}\right) - n\left(\mathbf{x}, \frac{\sigma}{\sqrt{\log(4)}}\right) \right).$$

Here, we have scaled and resized the Gaussians so that the impulse response at the origin is normalized to $m(\mathbf{0}, \sigma) = 1$ so that the zero-crossings of the Mexican hat filter lie on a circle of radius σ, for example, with $m((\sigma, 0), \sigma) = 0$ and so that m is strictly high pass with $\int_{\mathbb{R}^2} m(\mathbf{x}, \sigma) \, dx_1 \, dx_2 = 0$.

APPENDIX B

PARAMETRIC FORM

Our ellipse parameterization does not make use of several elements that are traditionally associated with such curves. We propose in this and in the next appendices a few formulas that make the link between $(\mathbf{p}, \mathbf{q}, \mathbf{r})$ and other relevant quantities.

Any coordinate $\mathbf{x} \in \partial\Gamma$ satisfies

$$\mathbf{x}(\theta) = \mathbf{g} + \mathbf{c} \, \cos\theta + \mathbf{s} \, \sin\theta,$$

where $\theta \in [-\pi, \pi]$ is some free parameter and where

$$\mathbf{c} = \frac{2 \, \mathbf{p} - \mathbf{q} - \mathbf{r}}{3},$$
$$\mathbf{s} = \frac{\mathbf{q} - \mathbf{r}}{\sqrt{3}}.$$

APPENDIX C

EXTREMAL POINTS

The extremal points of the ellipse are those where the curvature of $\partial\Gamma$ is either minimum or maximum. They are given by

$$\theta_k = \frac{1}{2} \, \arctan\left(\frac{u}{v}\right) + k \, \frac{\pi}{2},$$

with $k \in \{0, 1, 2, 3\}$ and

$$u = q_1 \, (2 \, p_1 - q_1) + q_2 \, (2 \, p_2 - q_2)$$
$$\quad - r_1 \, (2 \, p_1 - r_1) - r_2 \, (2 \, p_2 - r_2),$$
$$v = \sqrt{3} \, \left(p_1^2 - 3 \, g_1^2 + p_2^2 - 3 \, g_2^2 + 2 \, (q_1 \, r_1 + q_2 \, r_2)\right).$$

APPENDIX D

ORIENTATION

The orientation of the ellipse with respect to the system of coordinates is

$$\phi = \arctan\left(\frac{a_2}{a_1}\right),$$

with

$$\mathbf{a} = \mathbf{s} \, \sqrt{\sqrt{u^2 + v^2} - v} + \text{sgn}(e_{12}) \, \mathbf{c} \, \sqrt{\sqrt{u^2 + v^2} + v}.$$

APPENDIX E

ECCENTRICITY

Calling a the semimajor axis of the ellipse and b its semiminor axis, we have that

$$a = \sqrt{\frac{2}{27}} \, \sqrt{e_{11} + e_{22} + \sqrt{(e_{11} + e_{22})^2 - 27 \, \alpha^2}},$$
$$b = \sqrt{\frac{2}{27}} \, \sqrt{e_{11} + e_{22} - \sqrt{(e_{11} + e_{22})^2 - 27 \, \alpha^2}}.$$

The eccentricity of the ellipse is then $\varepsilon = \sqrt{1 - \frac{b^2}{a^2}}$.

APPENDIX F

PARAMETRIC CONVERSION

Let an ellipse be described by its center $\mathbf{g}$, its semimajor and semiminor axes a and b, and the tilt ϕ of its semimajor axis with respect to the horizontal axis $\mathbf{e}_1$. Then, a fully regularized set of points $\{\mathbf{p}, \mathbf{q}, \mathbf{r}\}$ can be constructed as

$$\begin{cases} p_1 = g_1 + a \, \cos\gamma \, \cos\phi - b \, \sin\gamma \, \sin\phi, \\ p_2 = g_2 + a \, \cos\gamma \, \sin\phi + b \, \sin\gamma \, \cos\phi, \\ q_1 = g_1 + a \, \cos\left(\gamma + \frac{3\,\pi}{2}\right) \cos\phi - b \, \sin\left(\gamma + \frac{3\,\pi}{2}\right) \sin\phi, \\ q_2 = g_2 + a \, \cos\left(\gamma + \frac{3\,\pi}{2}\right) \sin\phi + b \, \sin\left(\gamma + \frac{3\,\pi}{2}\right) \cos\phi, \\ r_1 = g_1 + a \, \cos\left(\gamma - \frac{3\,\pi}{2}\right) \cos\phi - b \, \sin\left(\gamma - \frac{3\,\pi}{2}\right) \sin\phi, \\ r_2 = g_2 + a \, \cos\left(\gamma - \frac{3\,\pi}{2}\right) \sin\phi + b \, \sin\left(\gamma - \frac{3\,\pi}{2}\right) \cos\phi, \end{cases}$$

with $p_3 = q_3 = r_3 = 1$ and

$$\gamma = \text{sgn}(\cos\phi) \, \arccos\left(\frac{a \, \sin\phi}{\sqrt{(a \, \sin\phi)^2 + (b \, \cos\phi)^2}}\right),$$

which ensures $q_2 = r_2$.

APPENDIX G

FOCI

The focal points of the ellipse are $(\mathbf{g} + \mathbf{f})$ and $(\mathbf{g} - \mathbf{f})$, with $\mathbf{f} = (f_1, f_2, 0)$ and

$$f_1 = \text{sgn}(e_{12}) \, a \, \sqrt{\frac{a^2 \, e_{22} - \alpha^2}{a^2 \, (e_{11} + e_{22}) - \alpha^2}},$$
$$f_2 = -a \, \sqrt{\frac{a^2 \, e_{11} - \alpha^2}{a^2 \, (e_{11} + e_{22}) - \alpha^2}}.$$

APPENDIX H

PERIMETER

The exact perimeter of an ellipse must be expressed with nontraditional functions aptly called elliptic integrals. The following excellent approximation has been proposed by Ramanujan:

$$|\partial\Gamma| \approx \pi \, (a + b) \left(1 + \frac{3 \, h}{10 + \sqrt{4 - 3 \, h}}\right),$$

with $h = ((a - b)/(a + b))^2$.

ACKNOWLEDGMENTS

REFERENCES

[1] P. Thévenaz and M. Unser, "Snakuscules," *IEEE Trans. Image Processing,* vol. 17, no. 4, pp. 585-593, Apr. 2008.

[2] S. Tsuji and F. Matsumoto, "Detection of Ellipses by a Modified Hough Transformation," *IEEE Trans. Computers,* vol. 27, no. 8, pp. 777-781, Aug. 1978.

[3] R. McLaughlin and M. Alder, "The Hough Transform versus the UpWrite," *IEEE Trans. Pattern Analysis and Machine Intelligence,* vol. 20, no. 4, pp. 396-400, Apr. 1998.

[4] N. Bennett, R. Burridge, and N. Saito, "A Method to Detect and Characterize Ellipses Using the Hough Transform," *IEEE Trans. Pattern Analysis and Machine Intelligence,* vol. 21, no. 7, pp. 652-657, July 1999.

[5] A. Garrido and N. Pérez de la Blanca, "Applying Deformable Templates for Cell Image Segmentation," *Pattern Recognition,* vol. 33, no. 5, pp. 821-832, May 2000.

[6] J. Blokland, A. Vossepoel, A. Bakker, and E. Pauwels, "Delineating Elliptical Objects with an Application to Cardiac Scintigrams," *IEEE Trans. Medical Imaging,* vol. 6, no. 1, pp. 57-66, Mar. 1987.

[7] D. Bright and E. Steel, "Two-Dimensional Top Hat Filter for Extracting Spots and Spheres from Digital Images," *J. Microscopy,* vol. 146, no. 2, pp. 191-200, May 1987.

[8] P. Lipson, A. Yuille, D. O'Keeffe, J. Cavanaugh, J. Taaffe, and D. Rosenthal, "Deformable Templates for Feature Extraction from Medical Images," *Proc. First European Conf. Computer Vision,* pp. 413-417, Apr. 1990.

[9] F. Escolano, M. Cazorla, D. Gallardo, and R. Rizo, "Deformable Templates for Tracking and Analysis of Intravascular Ultrasound Sequences," *Proc. Int'l Workshop Energy Minimization Methods in Computer Vision and Pattern Recognition,* pp. 521-534, May 1997.

[10] M. Kass, A. Witkin, and D. Terzopoulos, "Snakes: Active Contour Models," *Proc. First IEEE Int'l Conf. Computer Vision,* pp. 259-268, June 1987.

[11] B. Bascle and R. Deriche, "Features Extraction Using Parametric Snakes," *Proc. 11th Int'l Conf. Pattern Recognition,* pp. 659-662, Aug.-Sept. 1992.

[12] Y.-L. Fok, C. Chan, and T. Chin, "Automated Analysis of Nerve-Cell Images Using Active Contour Models," *IEEE Trans. Medical Imaging,* vol. 15, no. 3, pp. 353-368, June 1996.

[13] J. Cabrera and P. Meer, "Unbiased Estimation of Ellipses by Bootstrapping," *IEEE Trans. Pattern Analysis and Machine Intelligence,* vol. 18, no. 7, pp. 752-756, July 1996.

[14] A. Fitzgibbon, M. Pilu, and R. Fisher, "Direct Least Square Fitting of Ellipses," *IEEE Trans. Pattern Analysis and Machine Intelligence,* vol. 21, no. 5, pp. 476-480, May 1999.

[15] K. Voss and H. Suesse, "A New One-Parametric Fitting Method for Planar Objects," *IEEE Trans. Pattern Analysis and Machine Intelligence,* vol. 21, no. 7, pp. 646-651, July 1999.

[16] J. Guerrero, S. Salcudean, J. McEwen, B. Masri, and S. Nicolaou, "Real-Time Vessel Segmentation and Tracking for Ultrasound Imaging Applications," *IEEE Trans. Medical Imaging,* vol. 28, no. 8, pp. 1079-1090, Aug. 2007.

[17] N. Kharma, H. Moghnieh, J. Yao, Y. Guo, A. Abu-Baker, J. Laganiere, G. Rouleau, and M. Cheriet, "Automatic Segmentation of Cells from Microscopic Imagery Using Ellipse Detection," *IET Image Processing,* vol. 1, no. 1, pp. 39-47, Mar. 2007.

[18] C. Yap and H. Lee, "Identification of Cell Nucleus Using a Mumford-Shah Ellipse Detector," *Proc. Fourth Int'l Symp. Visual Computing,* pp. 582-593, Dec. 2008.

[19] E. Dura, J. Bell, and D. Lane, "Superellipse Fitting for the Recovery and Classification of Mine-Like Shapes in Sidescan Sonar Images," *IEEE J. Oceanic Eng.,* vol. 33, no. 4, pp. 434-444, Oct. 2008.

[20] H. Li, D. Chen, and Q. Yang, "Image Processing Technique for Characteristic Test of Cell Based on Electrorotation Chip," *Proc. Second Int'l Conf. Bioinformatics and Biomedical Eng.,* vol. 2, pp. 2526-2529, May 2008.

[21] D. Pedoe, "Thinking Geometrically," *The Am. Math. Monthly,* vol. 77, no. 7, pp. 711-721, Aug.-Sept. 1970.

[22] L. Shepp and B. Logan, "The Fourier Reconstruction of a Head Section," *IEEE Trans. Nuclear Science,* vol. 21, no. 3, pp. 21-43, June 1974.

[23] J. Wuest, E. Denarié, E. Brühwiler, L. Tamarit, M. Kocher, and E. Gallucci, "Tomography Analysis of Fiber Distribution and Orientation in Ultra High-Performance Fiber-Reinforced Composites with High-Fiber Dosages," *Experimental Techniques,* Sept./Oct. 2008.

Philippe Thévenaz graduated in January 1986 from the École polytechnique fédérale de Lausanne (EPFL), Switzerland, with a diploma in microengineering. He received the PhD degree in June 1993, with a thesis on the use of the linear prediction residue for text-independent speaker recognition. Before that, he was with the Institute of Microtechnology (IMT) of the University of Neuchâtel, Switzerland, where he worked in the domain of image processing (optical flow) and speech processing (speech coding and speaker recognition). Later, he was a visiting fellow with the Biomedical Engineering and Instrumentation Program, US National Institutes of Health (NIH), Bethesda, Maryland, where he developed research interests that include splines and multiresolution signal representations, geometric image transformations, and biomedical image registration. Since 1998, he has been with the EPFL as a senior researcher. He is a member of the IEEE.

Ricard Delgado-Gonzalo received the equivalent of an MSc degee in telecommunications engineering and the equivalent of an MSc degree in mathematics from the Universitat Politècnica de Catalunya (UPC) in 2006 and 2007, respectively. In 2008, he joined the Biomedical Imaging Group at the École polytechnique fédérale de Lausanne (EPFL), Switzerland, as a PhD student and assistant, where he currently works on applied problems related to image reconstruction, segmentation, and tracking, as well as on the mathematical foundations of signal processing and spline theory. He is a student member of the IEEE.

Michael Unser received the MS (summa cum laude) and PhD degrees in electrical engineering in 1981 and 1984, respectively, from the École polytechnique fédérale de Lausanne (EPFL), Switzerland. From 1985 to 1997, he worked as a scientist with the US National Institutes of Health, Bethesda, Maryland. He is now a full professor and director of the Biomedical Imaging Group at the EPFL. His main research area is biomedical image processing. He has a strong interest in sampling theories, multiresolution algorithms, wavelets, and the use of splines for image processing. He has published more than 150 journal papers on those topics, and is one of ISI's highly cited authors in engineering (http://isihighlycited.com). He has held the position of associate editor-in-chief (2003-2005) for the *IEEE Transactions on Medical Imaging* and has served as an associate editor for the same journal (1999-2002, 2006-2007), the *IEEE Transactions on Image Processing* (1992-1995), and *IEEE Signal Processing Letters* (1994-1998). He is currently a member of the editorial boards of *Foundations and Trends in Signal Processing*, the *SIAM Journal of Imaging Sciences*, and *Sampling Theory in Signal and Image Processing*. He coorganized the First IEEE International Symposium on Biomedical Imaging (ISBI '02) and was the founding chair of the technical committee of the IEEE-SP Society on Bio Imaging and Signal Processing (BISP). He received the 1995 and 2003 Best Paper Awards, the 2000 Magazine Award, and the 2008 Technical Achievement Award from the IEEE Signal Processing Society. He is an EURASIP fellow and a member of the Swiss Academy of Engineering Sciences. He is a fellow of the IEEE.